

Radiation-Hydrodynamical Simulations of Pulsational Pair-Instability Supernovae

Ke-Jung Chen^{1*}, Daniel J. Whalen², Weiqun Zhang³, and S. E. Woosley⁴

¹ *Institute of Astronomy and Astrophysics, Academia Sinica, Taipei 10617, Taiwan*

² *Institute of Cosmology and Gravitation, Portsmouth University, Portsmouth, UK*

³ *Center for Computational Sciences and Engineering, Lawrence Berkeley National Lab, Berkeley, CA 94720, USA*

⁴ *Department of Astronomy and Astrophysics, University of California at Santa Cruz, Santa Cruz, CA 95060, USA*

23 March 2022

ABSTRACT

Stars with masses of 80 - 130 M_{\odot} can encounter the pair instability at the end of their lives, which can trigger consecutive episodes of explosive thermonuclear burning and the ejection of a series of massive shells. Collisions between these shells produce bright transients known as pulsational pair-instability supernovae (PPI SNe) that may account for some superluminous supernovae (SLSNe). Here we report new 2D and 3D radiation hydrodynamical simulations of PPI SNe performed with **CASTRO**. Radiation transport leads to the formation of hot spots in the ejecta that boost the luminosity of the event by up to a factor of three over 1D models and cause it to vary by up to 30% with viewing angle. Luminosities peak at $\sim 2 \times 10^{43}$ erg s⁻¹ for 50 - 100 days and then fall to $\sim 3 \times 10^{42}$ erg s⁻¹ for 100 - 200 days before finally fading. Although radiation also suppresses mixing during the collision by preventing the formation of a reverse shock in the thin shell, line emission from ¹²C and ¹⁶O in the final pulse along with the absence of ²⁸Si and ⁵⁶Fe lines could characterize these transients as PPI SNe in future surveys by the *Vera Rubin Telescope*, the *Nancy Grace Roman Space Telescope*, and *Euclid*.

Key words:

supernovae: general – stars: supernovae – nuclear reactions – radiative transfer– hydrodynamics – instabilities

1 INTRODUCTION

Stars with masses $\gtrsim 80 M_{\odot}$ can build up helium cores exceeding 35 M_{\odot} that can encounter the pair instability late in their lives, in which thermal photons are converted into positron-electron pairs at the expense of pressure support of the core against collapse. Pair creation softens the adiabatic index of the gas, γ , which falls below 4/3 and causes the core to contract. Core contraction raises its temperature and can ignite rapid carbon burning that does not unbind the star but causes it to pulsate with a period of a few hundred seconds, producing a series of sonic waves that propagate through the star. As the helium core grows in mass the eruptions become more energetic but have less mass, and the interval between them increases to several years.

The eruptions can produce a supernova (SN)-like transient at helium core masses above 45 M_{\odot} . The first strong pulse has energies of $10^{49} - 10^{50}$ erg that can easily eject

the hydrogen envelope, whose binding energy is $10^{43} - 10^{44}$ erg, and produce a faint Type IIP SN. However, subsequent pulses colliding with the first can produce a much brighter Type IIn SN. If no hydrogen envelope remains at the time of the eruptions, collisions between consecutive helium shells ejected by the pulsations can produce a luminous Type I SN. For helium core masses of 45 – 55 M_{\odot} , the interval between pulsations becomes several years and the shells collide at radii of $10^{15} - 10^{16}$ cm if they have velocities of ~ 1000 km s⁻¹. In these circumstances, much of the collision energy is dissipated as optical emission known as a pulsational pair-instability supernova (PPI SN; Barkat et al. 1967; Woosley et al. 2007; Woosley 2017).

The energetic collision of a 10^{51} erg pulse can make a superluminous SN (Inserra et al. 2016; Takahashi 2018; Gal-Yam 2019; Chen 2021, SLSN) such as SN 2006gy and SN 2007bi. Recent stellar evolution models by Woosley (2017) and Leung et al. (2019) confirmed a broad variety of outcomes for PPI SNe and calculations of their light curves have shown that they can produce events from multiple faint SNe

* E-mail: kjchen@asiaa.sinica.edu.tw

to a single SLSN (Woosley et al. 2007; Dessart et al. 2015; Moriya & Langer 2015; Whalen et al. 2014; Jerkstrand et al. 2016; Woosley 2017). Woosley et al. (2007) modeled the PPI SN of a $110 M_{\odot}$ solar-metallicity star to explain the light curve of SN 2006gy. The newly discovered SN IPTF14hls (Arcavi 2017) has a long-duration and a multi-peak light curve that could be due to collisions between multiple shells in a PPI SN (Woosley 2018).

However, in 1D simulations of these events much of the luminosity originates from a large density spike due to a thin, dense shell that forms during the collision that in reality would be subject to fragmentation and clumping in 3D by hydrodynamical instabilities. 2D hydrodynamical simulations of a PPI SN by Chen et al. (2014) have shown that the development of Rayleigh-Taylor (RT) instabilities drives mixing between the colliding shells, breaking apart the dense shell. This study could not evaluate the effect of the instabilities on the light curve or spectra of the event because it did not include radiation hydrodynamics, which is required not only to properly model radiation flow through the ejecta but to capture its true structure because of the strong coupling between gas flows and the radiation. Realistic light curve calculations for PPI SNe must therefore be performed in at least 2D with a mesh that is fine enough to resolve the thin radiating regions of the collisions.

We have performed multidimensional radiation-hydrodynamical simulations of a PPI SN with the **CASTRO** code to study how radiation flows alter the structure of the dense shell and how instabilities affect the light curve of the collision. We performed 1D, 2D, and 3D simulations for comparison with previous hydrodynamics simulations and to study the effect of dimensionality on the light curve. We describe our **CASTRO** models in Section 2 and present our 1D, 2D, and 3D models in Sections 3, 4, and 5, respectively. We discuss the spectral signatures of these events, which include the effects of multidimensional mixing, in Section 6 and conclude in Section 7.

2 NUMERICAL METHOD

Our **CASTRO** simulation is initialized with the $110 M_{\odot}$ solar-metallicity progenitor that was studied with **KEPLER** by Woosley et al. (2007), Whalen et al. (2014), and Chen et al. (2014).

2.1 KEPLER Progenitor Model

Although the star has solar metallicity, mass loss was suppressed over its lifetime in **KEPLER** (Weaver et al. 1978; Woosley et al. 2002) to approximate the evolution of a primordial (Pop III) star. It therefore still has a mass of $74.6 M_{\odot}$ with a $49.9 M_{\odot}$ He core when it encounters the PI as a red supergiant, with a radius of 1.1×10^{14} cm and a luminosity of 9.2×10^{39} erg s⁻¹. The loss of thermal pressure support in the core due to the creation of $e^+ - e^-$ pairs causes it to contract, radiate neutrinos and light, and grow in temperature from $\sim 10^9$ K to 3.04×10^9 K, well above the usual 2.0×10^9 K at which O stably burns in massive stars. This rise in temperature triggers explosive nuclear burning that consumes $1.49 M_{\odot}$ of O and $1.55 M_{\odot}$ of C and releases 1.4×10^{51} erg. Most of the energy goes into expanding the

star but $\sim 10\%$ goes into the ejection of the weakly bound outer layers of the core and surrounding envelope ($24.5 M_{\odot}$, mostly He and some H). This first shell is ejected at peak velocities of ~ 1000 km s⁻¹. As shown in Figure 2 of Woosley et al. (2007), the expulsion of the envelope looks like a weak SN, with a brief breakout luminosity of 5×10^{42} erg s⁻¹ followed by a 7.9×10^{41} erg s⁻¹ plateau powered primarily by He recombination. We call this first ejection P1.

What remains after the initial outburst is a $50.7 M_{\odot}$ star that is only a little more massive than the original He core. It again contracts, emits neutrinos, becomes hotter, and encounters the PI 6.8 years after the first. The core ejects another shell into space that is less massive than P1, $5.1 M_{\odot}$, but more energetic, 6.0×10^{50} erg. We call this shell P2, and it is then followed by an even less massive but somewhat faster shell, P3, that quickly overtakes it and collides with it. Nine years later the core contracts a final time and enters a stable Si burning phase that forms an Fe core that later collapses. If the core is rapidly rotating it could produce a rapidly-spinning neutron star (a millisecond magnetar; e.g., Metzger et al. 2011) or a black hole accretion disk system (a collapsar; e.g., MacFadyen & Woosley 1999) that could result in a gamma-ray burst (Whalen et al. 2008; Mesler et al. 2012, 2014), but we do not consider such events here.

We map the 1D **KEPLER** profiles of this star into **CASTRO** at the time P3 is launched and the forward shock of P1 is at $r \sim 5 \times 10^{16}$ cm (the black plot in Figure 1). The explosion was then evolved until the forward shock of P3 is at $r \sim 10^{16}$ cm, after most of the thermal energy from its collision with P2 has been dissipated by radiative cooling (Woosley et al. 2007). Thus, here we only consider the collision of P2 and P3.

2.2 CASTRO

CASTRO is a multidimensional adaptive mesh refinement (AMR) radiation hydrodynamics code for astrophysical simulations (Almgren et al. 2010). It uses an unsplit piecewise-parabolic method (PPM) hydro scheme (Woodward & Colella 1984) to avoid spurious noise due to dimensional splitting, and has multi-species advection. We use a gamma law equation of state (EOS) and take $\gamma = 5/3$ for an ideal gas, which is a good description of the shells. The densities, velocities, temperatures, and elemental mass fractions from the 1D **KEPLER** model are mapped onto the AMR grids in **CASTRO** with the conservative scheme developed by Chen et al. (2011), which preserves physical quantities such as energy and mass during the mapping. The self-gravity of the ejecta is calculated with a monopole approximation by constructing a 1D gravitational potential from the radial average of the density and then using it to determine gravitational forces on all the AMR grids. This approximation is reasonable because there are no serious departures from spherical symmetry in the ejecta in our model. Although the **KEPLER** model includes the gravity of the compact remnant left after the final pulsation we do not include it in **CASTRO** because all three pulses have become gravitationally unbound by the time they are mapped onto the grid. We track ¹H, ⁴He, ¹²C, and ¹⁶O in the ejecta and neglect other species such as ²⁸Si, ⁴⁰Ca, ⁴⁴Ti, and ⁵⁶Ni because they are

mostly absent because the eruptions in the $110 M_{\odot}$ star are mainly driven by central ^{12}C burning.

2.3 Radiation Hydrodynamics

CASTRO solves two-temperature, multi-group flux-limited diffusion (MGFLD) radiation hydrodynamics (RHD) in which gas temperatures can be different from radiation temperatures, i.e., $E_r \neq aT_{\text{gas}}^4$. **CASTRO** adopts a mixed frame solution to the RHD equations assuming local thermodynamic equilibrium (LTE; Zhang et al. 2011, 2013). It uses a second-order explicit Godunov method for the hyperbolic part of the system and a first-order backward Euler method for the parabolic part. RHD in **CASTRO** has been applied to a wide range of astrophysical phenomena such as neutrino-driven core-collapse (CC) SNe (Dolence et al. 2015) and shock breakout in SNe (Lovegrove et al. 2017). Here, we use the gray approximation based on a frequency-integrated formulation of the RHD equations. The mixed-frame approach in **CASTRO** is similar to that in **Orion** (Krumholz et al. 2007) and has the advantage of being strictly conservative in energy but is of limited use for line transport, which in any event cannot be accurately represented by the gray FLD used here. Compared with the two-moment approach, the FLD is computationally efficient and uses much less memory for MGFLD but does not reproduce shadowing effects well.

We use frequency and temperature independent opacities,

$$\kappa = \kappa_T, \quad (1)$$

where κ_T is the Thomson electron scattering opacity,

$$\kappa_T = 0.2(1 + X) \text{ cm}^2 \text{ g}^{-1}, \quad (2)$$

and X is the ionized hydrogen mass fraction. We consider $\kappa_T = 0.1, 0.2, 0.3,$ and 0.4 to sample the range of ionized fractions in the gas. Light curves (LCs) for PPI SNe are calculated by tallying radiation flux at the photosphere, where the photons become free-streaming,

$$L = 4\pi r_p^2 F_{\text{rad}}, \quad (3)$$

where L is the bolometric luminosity in erg s^{-1} , F_{rad} is the radiation flux in $\text{erg cm}^{-2} \text{ s}^{-1}$ and r_p is the radius of the photosphere, which we take to be the outer boundary of the simulation box.

2.4 Grid / Boundary Conditions

Our 1D **CASTRO** simulations are performed on a spherical coordinate grid with a reflecting and outflow boundary conditions at the inner and outer boundaries at $r = 0$ and 2×10^{16} cm, respectively. We use uniform grids with 1024, 4096, and 8192 zones to test different resolutions and opacities. Our 2D runs use a cylindrical coordinate grid in r and z . We simulate one quadrant of the star and set outflow and reflecting boundary conditions on the upper and lower boundaries in r and z , respectively. The root grid has 512^2 zones with up to three levels of refinement for an effective resolution of $4,096^2$ on a domain 2×10^{16} cm on a side. The grids are refined on gradients in density and velocity. Our 3D **CASTRO** simulations are done on a Cartesian coordinate

grid in x , y , and z . Here, we simulate the full star with a 4π geometry with the center of the star at $x = 0$, $y = 0$, and $z = 0$, and we apply outflow boundary conditions to all boundaries. The root grid has 512^3 zones and up to two levels of refinement for a maximum effective resolution of $2,048^3$ for a volume that is 2×10^{16} cm on a side.

3 1D PPI SN EVOLUTION

We show density, velocity, radiation energy density, and radiation flux profiles for the $\kappa = 0.2$, 8192-zone 1D PPI SN run in Figure 1. As P2 plows through the density tail of P1 it decelerates and shocks the gas, piling up the hot, thin, dense shell visible as the density spike ($< \delta\rho/\rho > \sim 1,000 - 2,000$) at 10^{15} cm five days after the ejection of P3. As P3 catches up to P2 from behind it also plows up its density tail and forms another thin shocked shell of gas at $\sim 6 \times 10^{14}$ cm, albeit with a smaller density jump of ~ 10 . As P2 and P3 accumulate gas a reverse shock forms, detaches from the forward shock, and backsteps into the flow in the frame of the forward shock. These shocks are visible as the secondary density spikes behind the main ones in both shells.

In the previous hydro-only simulation of Chen et al. (2014), P3 overtakes P2 in just 50 days and merges with it at $r \sim 2.3 \times 10^{15}$ cm before they both collide with P1. In our **CASTRO** radiation hydrodynamics simulation, photons diffusing from P2 and P3 radiatively cool the gas at the expense of the kinetic energy of the shocks and decelerate them. They consequently merge at $r \sim 5.1 \times 10^{15}$ cm at 130 days. This result is consistent with Whalen et al. (2014), who studied the same explosion in 1D with the **RAGE** and **SPECTRUM** codes (Gittings et al. 2008; Frey et al. 2013), but with over 100 times the resolution and OPLIB atomic opacities (Magee et al. 1995). They found that that P2 and P3 merge at 150 days at $r \sim 6 \times 10^{15}$ cm. The higher OPLIB opacities led to stronger radiative cooling, greater deceleration of the shock, and a larger final collision radius. We show a closeup of the density spike at 300 days, after P3 has merged with P2, in the run in Figure 2. It has a thickness of about 1.4×10^{14} cm and densities of $\sim 8 \times 10^{-16} \text{ g cm}^{-3}$ to $\sim 1.1 \times 10^{-12} \text{ g cm}^{-3}$, with a jump of $\sim 1,375$.

We show light curves (LCs) for the PPI SN in Figure 3. As shown in the lower two panels of Figure 1, most of the flux originates from the forward shock driven by P3. Unlike Type IIIn SNe, in which the collision between the ejecta and a circumstellar shell are more abrupt, collisions between pair pulsations are more gradual because the ejections have no distinct inner surface. Consequently, the forward shock of P3 becomes gradually brighter as it plows up P2, as shown in the LCs. In Figure 3 the LC peaks at 50 days at a little below $10^{43} \text{ erg s}^{-1}$ in the 8192 zone run with $X = 0$ because of pre-collision heating between P3 and P2, somewhat lower than found by Woosley et al. (2007) and Whalen et al. (2014): $3.6 \times 10^{43} \text{ erg s}^{-1}$ and $7 \times 10^{43} \text{ erg s}^{-1}$, respectively. These differences again are likely due to the more realistic opacities in these two studies. Approximately 90% of the kinetic energy of the collision of P3 and P2 is radiated away as they both advance from 10^{15} cm to 2×10^{16} cm. The second peak in the LCs in Figure 3 is due to the collision of P3 and P2 at 130 days. The peak occurs somewhat later because the collision is an extended event and because of

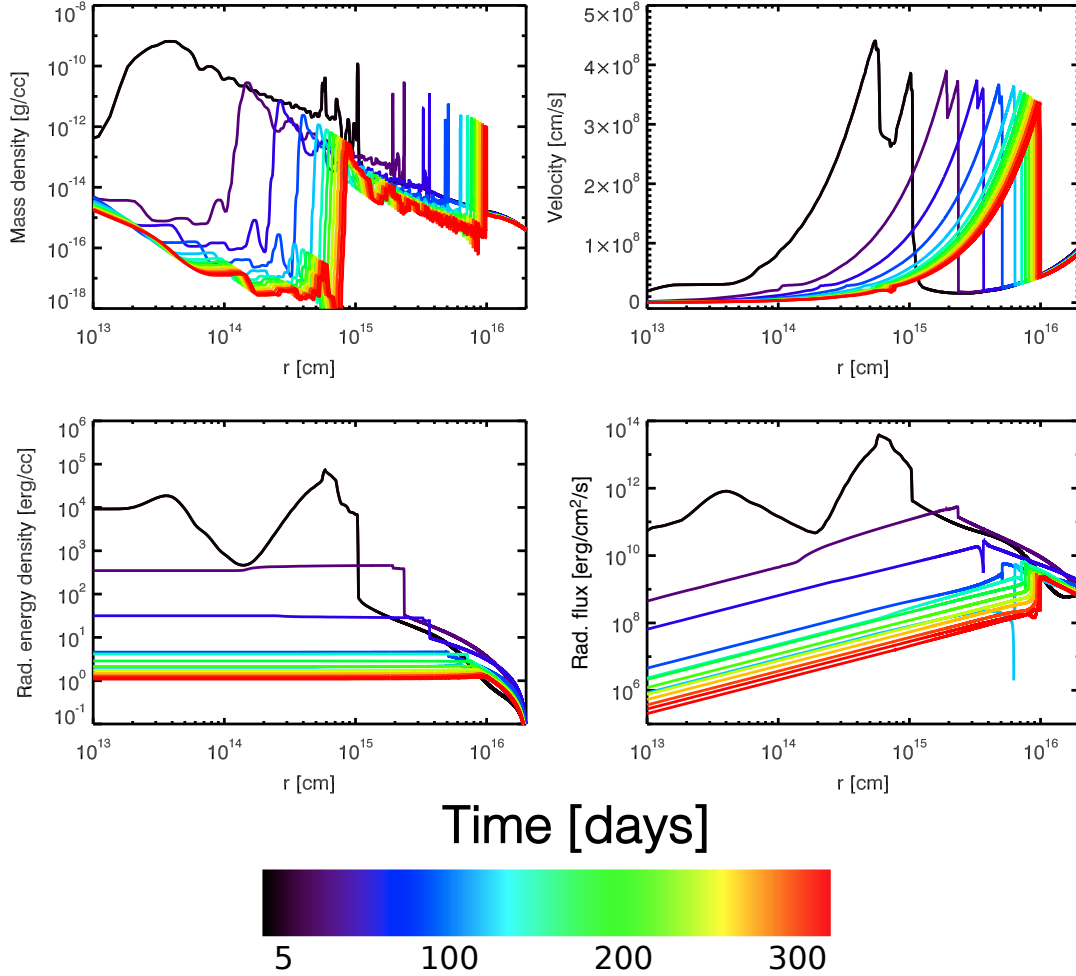


Figure 1. Gas densities, velocities, radiation energy densities, and radiation fluxes for the $\kappa = 0.2$, 8192-zone PPI SN model at 5 - 333 days after the ejection of P3. The collisions between P3 and P2 can be seen in the merging of the two velocity peaks over time.

the time it takes for photons due to the collision to diffuse out of the merged shell.

The LCs change with the number of grid zones because it determines how well the mesh resolves the structures that form in the flows before and after the collision of P3 and P2. These features govern the emission and transfer of photons across the grid. The 1024 zone LC has the highest peak luminosity and shortest duration. The second peak only appears in the LCs of the higher resolution runs, and the rise time of the second peak is earlier in the 4096 zone run. We show the effect of opacity on the LC in the lower panel of Figure 3. As the opacity increases, the two LC peaks become broader and dimmer, $7 - 11.5 \times 10^{42}$ erg s⁻¹ and durations of 150 - 200 days.

Our light curves are smoother than those in Woosley et al. (2007) and Whalen et al. (2014), which exhibit ripples due to the classic radiative instability described by Chevalier & Imamura (1982) and Imamura et al. (1984). As noted above, as P3 and P2 plow up gas a reverse shock forms, detaches from the forward shock, and backsteps into the flow in the frame of the forward shock. But if the post-shock gas can radiatively cool, as does the gas in Woosley et al. (2007) and Whalen et al. (2014), the reverse shock loses pressure support and recedes back toward the forward

shock. As the forward shock continues to plow up more material the cycle repeats. This oscillatory behavior imprints fluctuations in the LCs that we do not find here because of our lower Thomson scattering opacities. These features probably would not appear in a multidimensional simulation because the narrow region between the colliding shells in which the radiative instability occurs would likely be broken up by Rayleigh-Taylor (RT) instabilities, and reduce or remove altogether the fluctuations in the light curve.

Although we do not calculate spectra here, Whalen et al. (2014) found that at ~ 70 days the shock is hottest, ~ 5 eV or 55,000 K, and that its spectrum cuts off at about 500 Å, so P2 radiates strongly in the UV, like Type II_n SNe. After the collision, when more of the kinetic energy of the shells is dissipated, the shock cools and its spectrum softens to optical wavelengths. The PPI SN here is similar to the Type II_n SNe examined by Whalen et al. (2013) in that it is bright in the UV at early stages of the collision, when the shock has large radii, $\sim 10^{15}$ cm. This radius is similar to the inner radii of the shells of the Type II_n events in Whalen et al. (2013) when ejecta from the explosion crashes into them. With similar shock temperatures and radii upon collision, the initial total luminosities for PPI SNe and Type

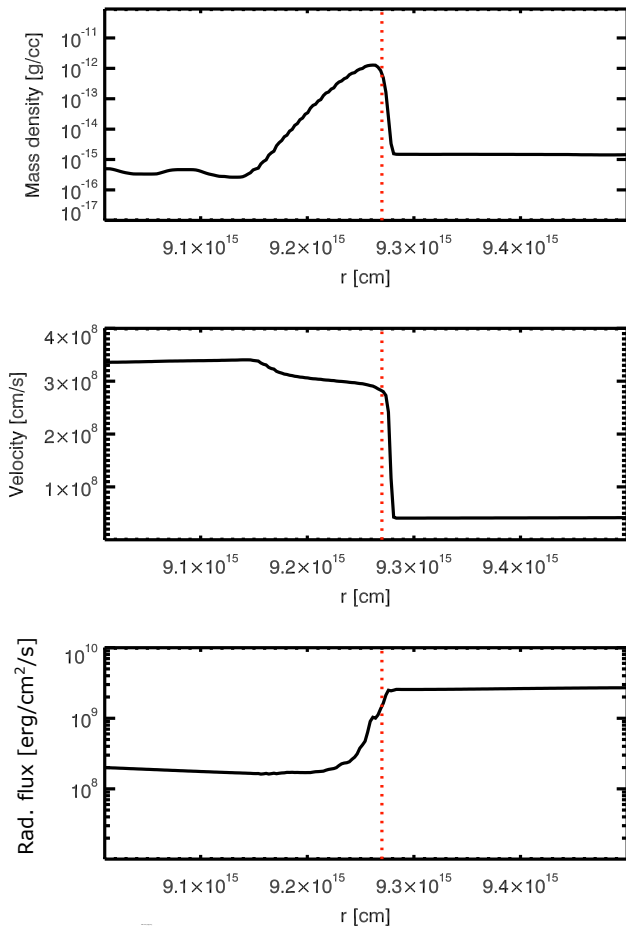


Figure 2. Zoom-in of the density spike at $t = 300$ days in the 8192 zone run. The red-dashed line marks the position of the forward shock of P3+P2. The spike is 1.4×10^{14} cm thick and is resolved by 50 zones.

line are comparable, as shown in Figure 2 in Whalen et al. (2013).

4 2D PPI SN EVOLUTION

We compare densities for the PPI SN at 50 days and 256 days with and without (Chen et al. 2014) radiation transport in Figure 4. The original spherical symmetry of both explosions has been broken by 50 days, although with significant differences in the morphologies of the ejecta. In the rad hydro model, radiation diffuses out of and cools the postshock gas, causing it to pile up in the thin dense shell visible at 2.05×10^{15} cm. Postshock radiative cooling decelerates the shell but also prevents the formation of a reverse shock that can create a pressure inversion that would lead to Rayleigh-Taylor (RT) instabilities. Deceleration delays the collision of P3 with P2 until well after 50 days in the rad hydro model but it happens at this time in the hydro only model. The collision in this latter model produces a reverse shock that triggers the formation of the prominent RT fingers at 1.9×10^{15} cm and strong mixing in the shell. There are some ripples in the thin shell in the rad hydro model due to the pref-

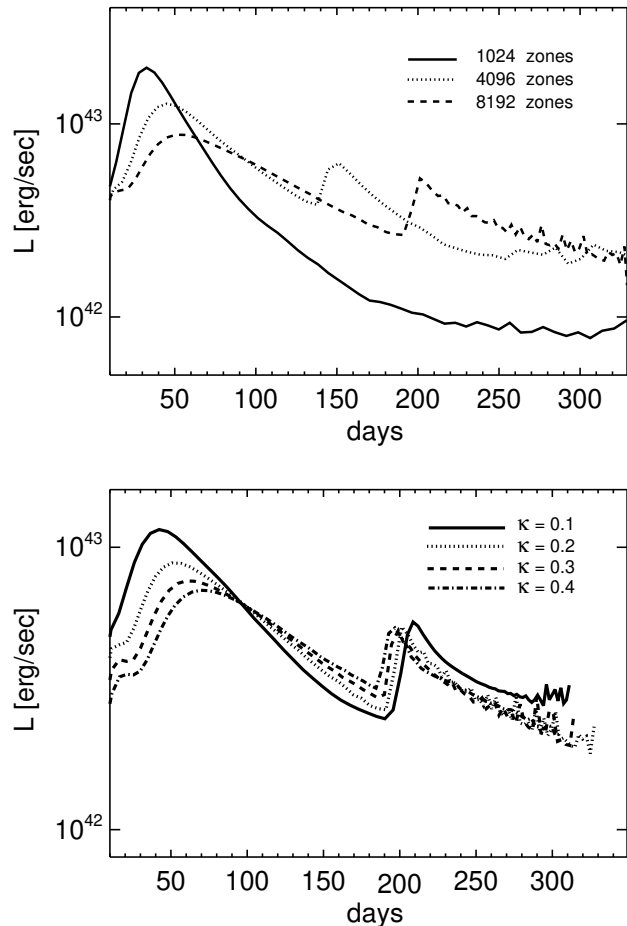


Figure 3. LCs for the 1D runs. Top: grid resolutions of 1024, 4096 and 8192 zones with $\kappa = 0.2$. Bottom: LCs for the 8192 zone run for $\kappa = 0.1 - 0.4$.

erential escape of radiation along lines of sight with lower optical depths, but they are minor and more reminiscent of Vishniac overstabilities than instabilities (Vishniac 1983).

By 256 days the shell has reached regions that are nearly optically thin, and its energy is rapidly dissipated because radiation easily diffuses from the shock. The deformations in the shell due to radiative cooling in the rad hydro model have grown somewhat in amplitude but are still smaller than the RT instabilities in the hydro only run. As shown in Figure 5, the amplitude of the ripples varies with opacity and is larger for lower opacities. This is due to the fact that radiation can escape through inhomogeneities in the thin shell at earlier times so the ripples appear and begin to grow sooner. Consequently, the dynamics of the shell depend on opacities to some degree. The $\kappa = 0.1$ shell is thicker than the $\kappa = 0.2$ shell because less efficient radiative cooling does not allow it to collapse to as high a density.

As the photosphere recedes into the combined P2+P3 shells, radiation emission becomes inhomogeneous and anisotropic as shown in Figure 6 and caused the PPI SN luminosity to vary with viewing angle. We show 2D LCs for $\kappa = 0.1, 0.2$ and 0.4 in Figure 7. For each opacity there are ten LCs for viewing angles $\theta = 0 - 90$ degrees that are coded by color. They differ from the 1D LCs in several respects.

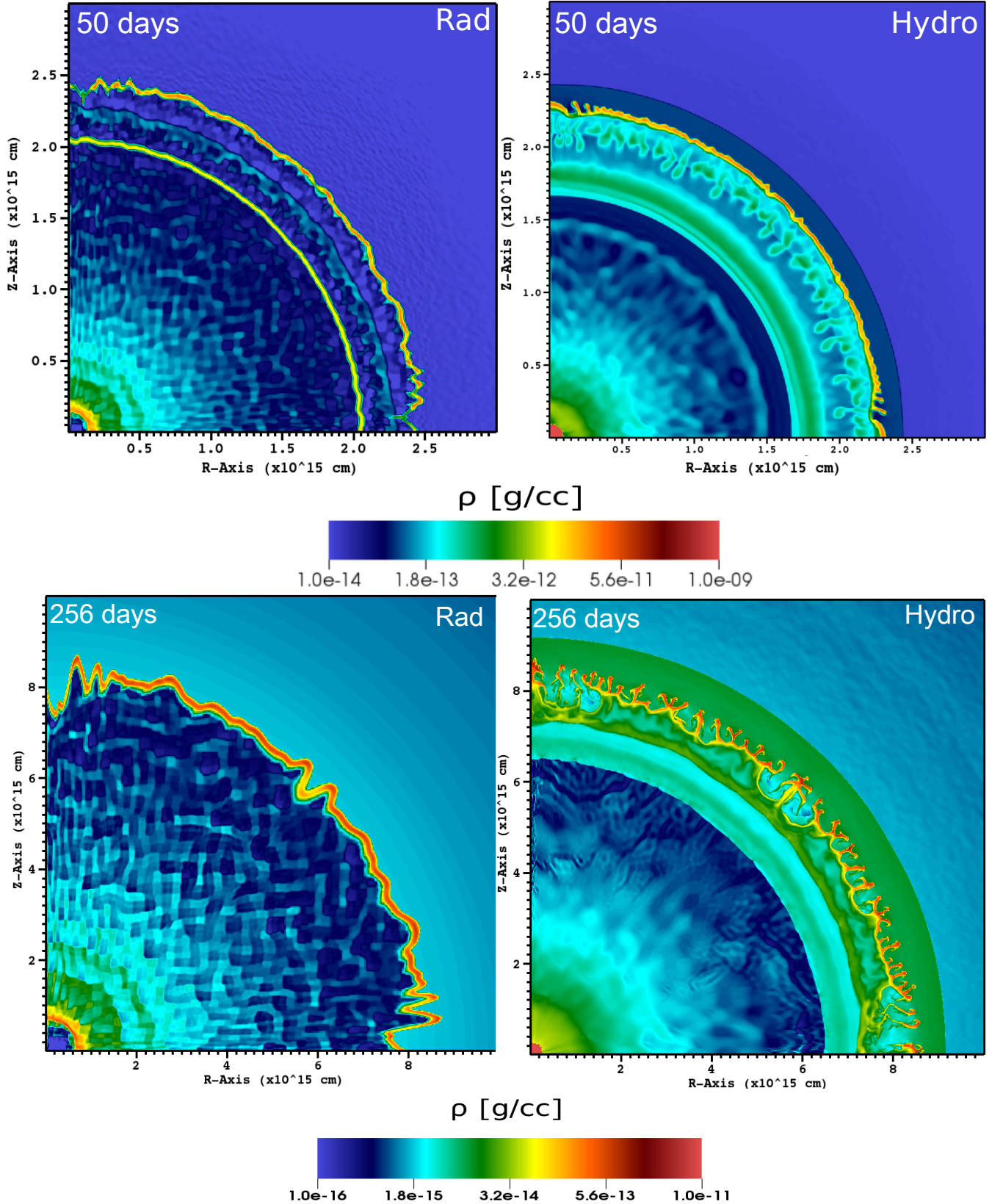


Figure 4. Density profiles for the $\kappa = 0.2$ radiation hydrodynamics run and previous pure hydrodynamic model at 50 and 256 days. In the former, the shock fails to produce a visible density discontinuity so the resulting fluid instabilities are weak. At 256 days, the hydro-only explosion exhibits prominent RT fingers in the postshock gas (the outer green arc).

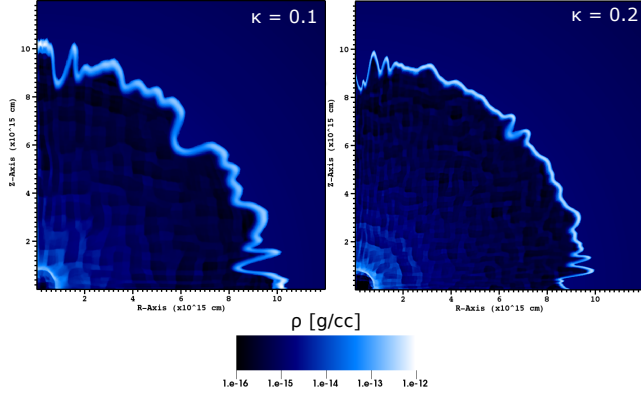


Figure 5. Deformations in the 2D thin shells in the $\kappa = 0.1$ and 0.2 runs 300 days after the collision of P3 and P2.

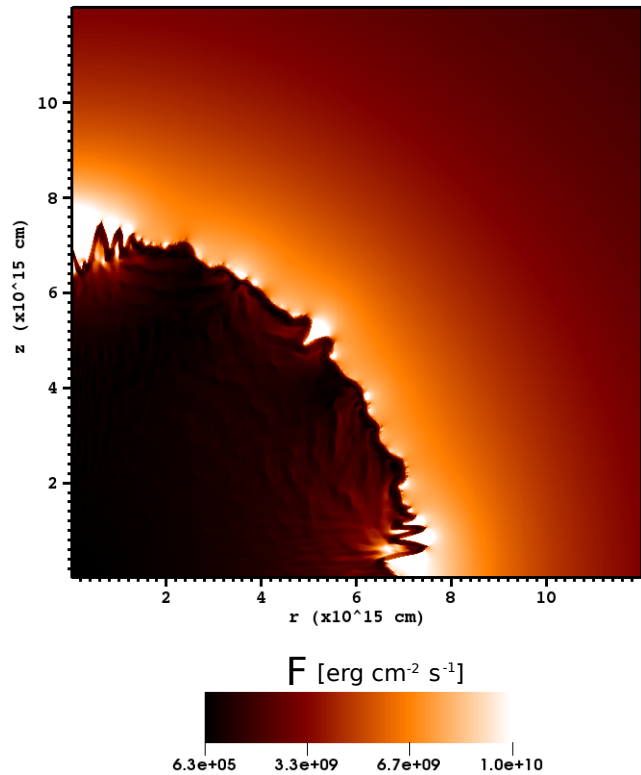


Figure 6. 2D radiation flux in the $\kappa = 0.2$ run at 212 days. Hot spots indicate large radiation fluxes and are randomly distributed across the merged shells, producing anisotropic emission from the event.

First, the peak luminosities for all the opacities exceed 10^{43} erg s $^{-1}$ and last for 50 - 120 days because of the hot spots in the shell. Consequently, the PPI SN is brighter in 2D than in 1D. Second, the peak due to the collision of P3 and P2 in the 1D LCs is smoothed out in 2D. The LCs become increasingly sensitive to viewing angle at later times, where variations in luminosity can be up to 30%.

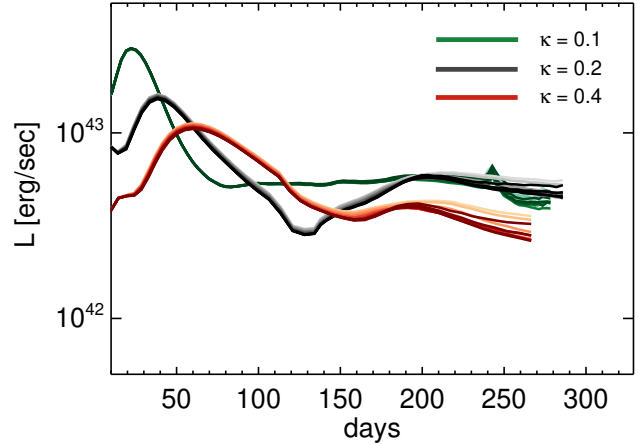


Figure 7. 2D PPI SN LCs calculated from the rad-hydro models with $\kappa = 0.1, 0.2,$ and 0.4 . For each opacity there are ten LCs from viewing angles $\theta = 0 - 90^\circ$ marked by a range of colors.

5 3D PPI SN EVOLUTION

We show density slices of the 2D and 3D rad hydro runs for $\kappa = 0.2$ at 250 days in Figure 8. The thin shells are at the same radii and they exhibit similar degrees of dimpling. However, the shell is thicker in the 3D run and the interior of the expanding remnant is more turbulent in 3D, which erases some of the fine structure in the interior of the 2D remnant. The irregularities in the surface of the 3D shell suggest that it too will exhibit hot spots with brighter emission, which is shown to be the case in Figure 9. Although there is more turbulence in the interior of the 3D remnant, its contribution to the total pressure does not appear to significantly change the expansion of the remnant because it has the same radius as the 2D remnant at 260 days.

LCs for the 3D explosion at different viewing angles are shown in Figure 10. They peak at $1.8 - 2.3 \times 10^{43}$ erg s $^{-1}$ and, as in the 2D explosion, lack the second peak in the 1D LCs. The peak lasts about 100 days before entering a plateau with $L \sim 2 - 3 \times 10^{42}$ erg s $^{-1}$. As the shell approaches the boundary of the box the flux again begins to vary strongly with viewing angle. The morphologies and LCs of the 2D and 3D are quite similar, suggesting that 2D simulations capture most of the features of the 3D runs at a fraction of the computational cost.

As originally suspected, the thin dense shell due to radiative cooling that forms in 1D simulations with radiation transport fractures into clumps in both 2D and 3D simulations of the same explosion but is still visible. We plot 1D angle-averaged density profiles for the 2D and 3D runs alongside the profile for the 1D run at 250 days for $\kappa = 0.1$ and 0.2 in the top panel of Figure 11. The 1D spike forms regardless of the chosen opacity with overdensities that exceed 1000 within a few days of formation. It splits into multiple bumps with overdensities of ~ 100 in the 2D and 3D explosions. Finer structures are present in the bumps for $\kappa = 0.2$. As noted earlier, the 3D shell is thicker than the 2D shell and has a smoother structure.

PPI SNe mostly eject elements lighter than ^{28}Si because of explosive carbon burning, and iron group elements such as ^{56}Ni that are often found in other types of SNe do not appear

[h]

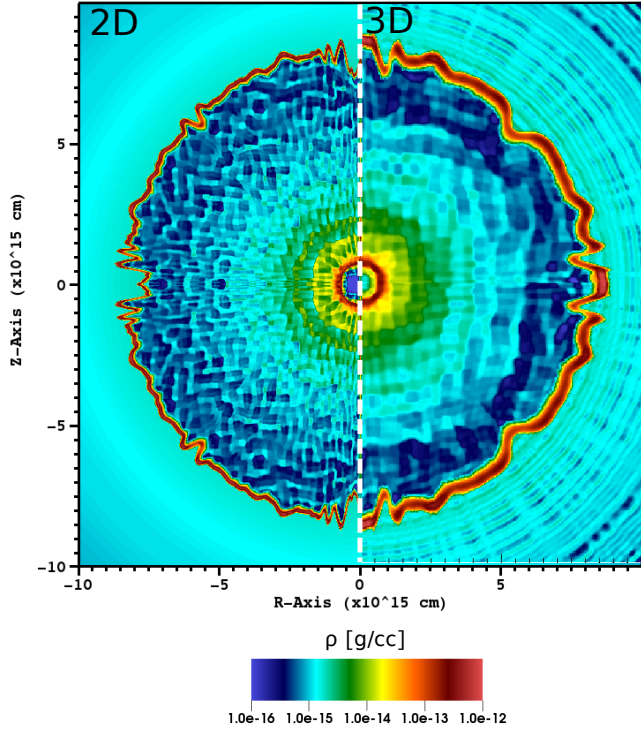


Figure 8. Density slices of the 2D and 3D PPI SNe at 250 days.

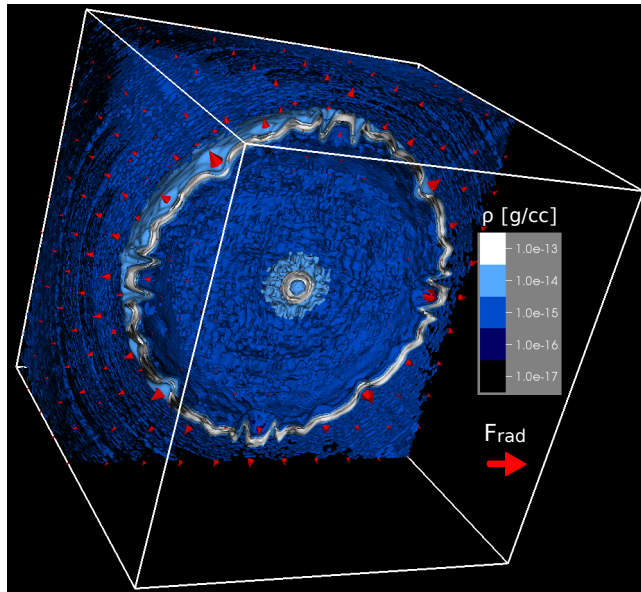


Figure 9. 3D density structure of the PPI SN and its radiation flux at 260 days. The box size is 10^{16} cm and the red arrows are radiation flux vectors.

in PPI explosions. We show angle-averaged mass fractions and velocities for the 2D $\kappa = 0.2$ run at 135 days in the bottom panel of Figure 11. The high ^{12}C and ^{16}O mass fractions interior to the thin shell are not due to mixing because radiative cooling dampens reverse shock formation and RT instabilities. They are instead primarily the ^{12}C and

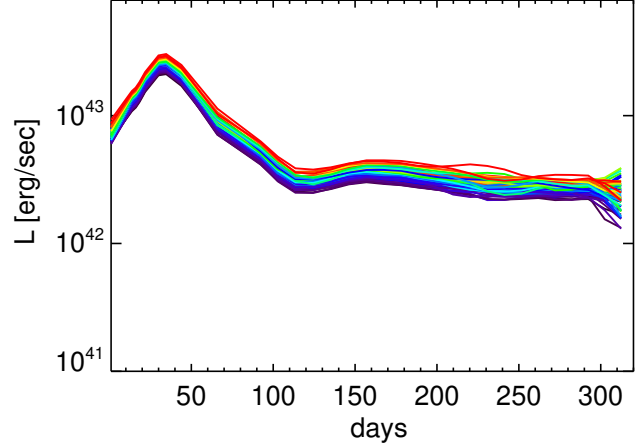


Figure 10. 3D PPI SN LCs. Colors represent 25 LCs from viewing angles $\theta = 0 - 180^\circ$ and azimuthal angles $\phi = 0 - 360^\circ$. The peak luminosity is $\sim 2 \times 10^{43}$ erg s^{-1} and lasts about 100 days.

^{16}O in P3 at the time of ejection. These elements mix with H and He in P2 only in the narrow band of radii ($< 5 \times 10^{14}$ cm) marked in dark grey in Figure 11 and would be visible to an external observer. Since ^{12}C and ^{16}O are dredged up to the front of the shock front, PPI SNe would be expected to exhibit strong ^{12}C and ^{16}O lines but few ^{28}Si or ^{56}Fe lines.

6 CONCLUSION

We find that multidimensional radiation hydrodynamical PPI SN simulations produce light curves that are up to three times brighter than those of 1D rad hydro models because radiative cooling leads to the formation of hot spots in the dense shell formed in the collision that emit more photons. Radiation hydrodynamics also suppresses mixing during the collision between pulses by cooling the thin shell and preventing the formation of a reverse shock. Peak bolometric luminosities for the $110 M_\odot$ PPI SN can reach $2 - 3 \times 10^{43}$ erg s^{-1} that can persist for 50 - 100 days in the rest frame of the event followed by a $2 - 3 \times 10^{42}$ erg s^{-1} plateau that lasts for 150 - 200 days. The hot spots that form from corrugations in the thin shell also introduce luminosities that vary with viewing angle, but only by up to $\sim 30\%$, a much smaller effect than the overall brightening of the explosion they produce. Although our models show that not much mixing occurs in PPI SNe, the collisions of P3 and P2 will produce ^{12}C and ^{16}O emission lines because P3 carries these species into the merged shell. This together with the absence of ^{28}Si and ^{56}Fe lines could be used to flag a transient as a PPI SN for further followup.

Temperature profiles for the PPI SN from Whalen et al. (2014) indicate that the shock reaches maximum temperatures of 50,000 - 100,000 K, not enough for the atoms to be completely ionized, so there will be bound-bound and bound-free contributions to the opacity in addition to the scattering opacities assumed here. Since opacity affects gas flows by regulating radiation flows, better opacities would produce more realistic light curves and spectra. Improved radiation transport schemes such as multigroup FLD can

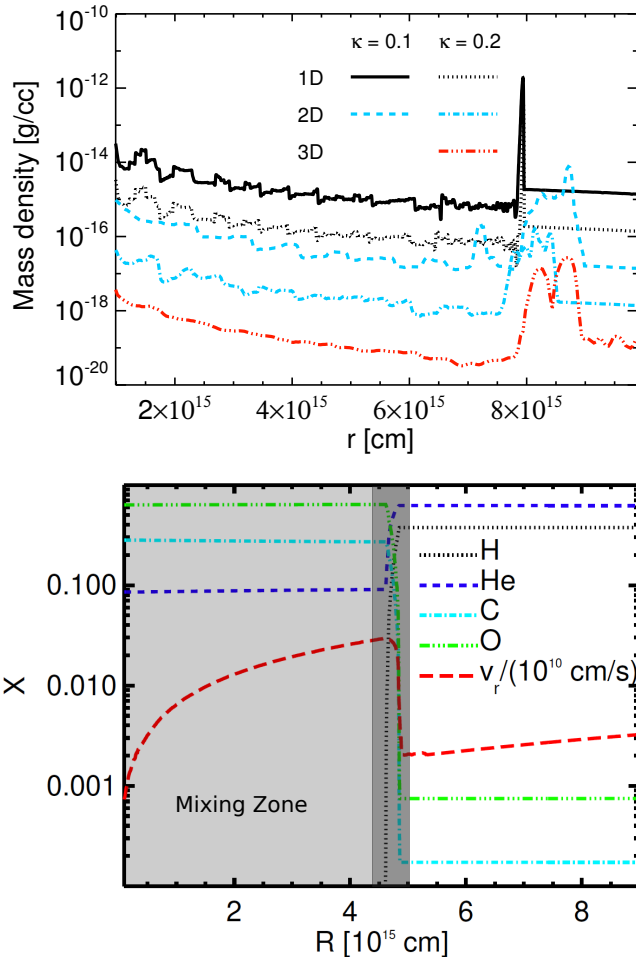


Figure 11. Top: angle-averaged density profiles for the 1D, 2D, and 3D $\kappa = 0.2$ runs at 250 days, each of which is offset by a factor of 10 for clarity. The density spike in 1D splits into one or more bumps in 2D and 3D. Bottom: angle-averaged mass fractions and velocities for the 2D rad hydro run at 135 days. The dark grey band marks the position of the dense shell and where ^{12}C and ^{16}O mix with ambient H and He.

also improve the quality of the LCs. In particular, higher-order schemes that approximate the angular distribution of the radiation such as implicit Monte Carlo (IMC), variable Eddington tensor formalism (VETF), or S_N methods would be better suited to the dense clumps in the disrupted shell because they capture shadowing better than FLD, in which radiation follows gradients in radiation energy densities and can cause flux to unphysically flow around obstacles. Such calculations would be more tractable in 2D, which our simulations suggest should be sufficient to capture most features in the radiating flows.

Here we have considered just a single PPI SN, but in future work we will expand our grid of simulations to include more progenitors from Woosley (2017) with improved radiation schemes and opacities to produce more realistic light curves and spectra. The detection and proper characterization of these transients will open new windows on massive star formation in the local and primordial universe. The advent of new SN factories such as the *Vera Rubin Telescope* and wide-field near infrared missions such as the *Nancy*

Grace Roman Space Telescope and *Euclid* will reveal more of these events and enlarge our understanding of PPI SNe and the deaths of other very massive stars in the coming decade.

ACKNOWLEDGEMENT

We thank Alex Heger, Dan Kasen, Ann Almgren, Mike Zingale, Lars Bildsten, and Ken Nomoto for many useful discussions. This research is supported by the Ministry of Science and Technology, Taiwan under grant no. MOST 110-2112-M-001-068-MY3 and the Academia Sinica, Taiwan under a career development award under grant no. AS-CDA-111-M04. K.C. thanks the Aspen Center for Physics, which is supported by NSF PHY-1066293, and the Kavli Institute for Theoretical Physics, which is supported by NSF PHY-1748958. Our numerical simulations were performed the National Energy Research Scientific Computing Center (NERSC), a U.S. Department of Energy Office of Science User Facility operated under Contract No. DE-AC02-05CH11231, the Center for Computational Astrophysics (CfCA) at National Astronomical Observatory of Japan (NAOJ), and the TIARA Cluster at the Academia Sinica Institute of Astronomy and Astrophysics (ASIAA).

Data Availability Statements: The simulation data underlying this article were generated from several large supercomputers. Due to the huge size of data volume, the derived data generated in this research will be shared on reasonable request to the corresponding author.

REFERENCES

- Almgren A. S., Beckner V. E., Bell J. B., Day M. S., Howell L. H., Joggerst C. C., Lijewski M. J., Nonaka A., Singer M., Zingale M., 2010, *ApJ*, 715, 1221
- Arcavi I. e. a., 2017, *Nat*, 551, 210
- Barkat Z., Rakavy G., Sack N., 1967, *Physical Review Letters*, 18, 379
- Chen K.-J., Heger A., Almgren A. S., 2011, *Computer Physics Communications*, 182, 254
- Chen K.-J., Woosley S., Heger A., Almgren A., Whalen D. J., 2014, *ApJ*, 792, 28
- Chen K.-J., 2021, *IJMPD*, 30, 2130001-164.
- Chevalier R. A., Imamura J. N., 1982, *ApJ*, 261, 543
- Dessart L., Audit E., Hillier D. J., 2015, *MNRAS*, 449, 4304
- Dolence J. C., Burrows A., Zhang W., 2015, *ApJ*, 800, 10
- Frey L. H., Even W., Whalen D. J., Fryer C. L., Hungerford A. L., Fontes C. J., Colgan J., 2013, *ApJS*, 204, 16
- Gal-Yam A., 2019, *ARA&A*, 57, 305.
- Gittings M., Weaver R., Clover M., Betlach T., Byrne N., Coker R., Dendy E., Hueckstaedt R., New K., Oakes W. R., Ranta D., Stefan R., 2008, *Computational Science and Discovery*, 1, 015005
- Imamura J. N., Wolff M. T., Durisen R. H., 1984, *ApJ*, 276, 667
- Inserra C., Bulla M., Sim S. A., Smartt S. J., 2016, *ApJ*, 831, 79

- Jerkstrand A., Smartt S. J., Heger A., 2016, *MNRAS*, 455, 3207
- Krumholz M. R., Klein R. I., McKee C. F., Bolstad J., 2007, *ApJ*, 667, 626
- Leung S.-C., Nomoto K., Blinnikov S., 2019, *ApJ*, 887, 72
- Lovegrove E., Woosley S. E., Zhang W., 2017, *ApJ*, 845, 103
- MacFadyen A. I., Woosley S. E., 1999, *ApJ*, 524, 262
- Magee N. H., Abdallah Jr. J., Clark R. E. H., Cohen J. S., Collins L. A., Csanak G., Fontes C. J., Gauger A., Keady J. J., Kilcrease D. P., Merts A. L., 1995, in S. J. Adelman & W. L. Wiese ed., *Astrophysical Applications of Powerful New Databases Vol. 78 of Astronomical Society of the Pacific Conference Series, Atomic Structure Calculations and New LOS Alamos Astrophysical Opacities*. p. 51
- Mesler R. A., Whalen D. J., Lloyd-Ronning N. M., Fryer C. L., Pihlström Y. M., 2012, *ApJ*, 757, 117
- Mesler R. A., Whalen D. J., Smidt J., Fryer C. L., Lloyd-Ronning N. M., Pihlström Y. M., 2014, *ApJ*, 787, 91
- Metzger B. D., Giannios D., Thompson T. A., Bucciantini N., Quataert E., 2011, *MNRAS*, 413, 2031
- Moriya T. J., Langer N., 2015, *A&A*, 573, A18
- Takahashi K., 2018, *ApJ*, 863, 153
- Vishniac E. T., 1983, *ApJ*, 274, 152
- Weaver T. A., Zimmerman G. B., Woosley S. E., 1978, *ApJ*, 225, 1021
- Whalen D., O'Shea B. W., Smidt J., Norman M. L., 2008, *ApJ*, 679, 925
- Whalen D. J., Even W., Lovekin C. C., Fryer C. L., Stiavelli M., Roming P. W. A., Cooke J., Pritchard T. A., Holz D. E., Knight C., 2013, *ApJ*, 768, 195
- Whalen D. J., Smidt J., Even W., Woosley S. E., Heger A., Stiavelli M., Fryer C. L., 2014, *ApJ*, 781, 106
- Woodward P., Colella P., 1984, *Journal of Computational Physics*, 54, 115
- Woosley S. E., 2017, *ApJ*, 836, 244
- Woosley S. E., 2018, *ApJ*, 863, 105
- Woosley S. E., Blinnikov S., Heger A., 2007, *Nat*, 450, 390
- Woosley S. E., Heger A., Weaver T. A., 2002, *Reviews of Modern Physics*, 74, 1015
- Zhang W., Howell L., Almgren A., Burrows A., Bell J., 2011, *ApJS*, 196, 20
- Zhang W., Howell L., Almgren A., Burrows A., Dolence J., Bell J., 2013, *ApJS*, 204, 7